Adjoint Solver-Based Analysis of Mouth-Tongue Morphologies on Vapor Deposition in the Upper Airway

Mohamed Talaat , Xiuhua Si , Jinxiang Xi *

Posted Date: 29 March 2024

doi: 10.20944/preprints202403.1863.v1

Keywords: morphological effect; adjoint solver; shape sensitivity; computational fluid dynamics (CFD); mucus-tissue layer; vapor transport; wall absorption; Acetaldehyde; Benzene

Article

Adjoint Solver-Based Analysis of Mouth-Tongue Morphologies on Vapor Deposition in the Upper Airway

Mohamed Talaat [1], Xiuhua Si [2] and Jinxiang Xi [1,*]

[1] Department of Biomedical Engineering, University of Massachusetts, Lowell, MA, 01854, USA; mohamed_talaat@student.uml.edu
[2] Department of Aerospace, Industrial, and Mechanical Engineering, California Baptist University, Riverside, CA, 92504, USA; asi@calbaptist.edu
* Correspondence: jinxiang_xi@uml.edu; Tel.: +1-978-934-3259

Abstract: Even though inhalation dosimetry is determined by three factors (i.e., breathing, aerosols, and the respiratory tract), the first two categories have been more widely studied than the last. Both breathing and aerosols are quantitative variables that can be easily changed, while respiratory airway morphologies are difficult to reconstruct, modify, and quantify. Despite several methods are available for model reconstruction and modification, developing an anatomically accurate airway model and morphing it to various physiological conditions remains labor-intensive and technically challenging. The objective of this study is to explore the feasibility of using an adjoint-CFD model to understand airway shape effects on vapor deposition and control vapor flux into the lung. A mouth-throat model was used, with the shape of the mouth and tongue being automatically varied via adjoint morphing, and the vapor transport being simulated using ANSYS Fluent coupled with a wall absorption model. Two chemicals with varying adsorption rates, Acetaldehyde and Benzene, were considered, which exhibited large differences in dosimetry sensitivity to airway shapes. For both chemicals, large shape deformations were explored to find the maximal possible morphing; both the maximal and intermediate deformations were simulated for morphology parametric studies. Results show that changing the mouth-tongue shape can alter the oral filtration by 3.2% for Acetaldehyde and 0.27% for Benzene under a given inhalation condition. This study demonstrates that the hybrid adjoint-CFD approach can be a practical and efficient method to investigate morphology-associated variability in inhalation dosimetry of vapors and nanomedicines.

Keywords: morphological effect; adjoint solver; shape sensitivity; computational fluid dynamics (CFD); mucus-tissue layer; vapor transport; wall absorption; Acetaldehyde; Benzene

1. Introduction

Respiratory morphology is a key component in predicting pulmonary drug delivery [1]. In contrast to extensive studies on aerosol properties (device and formulations) and breathing conditions (patients and delivery methods), studies of the effects of the respiratory tract and variability are scarce. Generating anatomically accurate airway models is still challenging and time-consuming. It is more challenging to generate representative airway models specific to different ages, genders, races, and diseases [2]. Furthermore, the respiratory tract is multiscale, from nose-mouth-throat, tracheobronchial, central airway, down to submicron alveoli [3]. The smaller the airway, the more difficult it is to reconstruct from images. The respiratory tract is compliant and can be dynamic during drug delivery. The drug aerosol transport and deposition involve multiple physics, including inertial impaction, diffusion, and sedimentation. Particle transport and deposition are highly sensitive to anatomical details, such as airway curvature, and disease-induced airway remodeling. Interactions between airway morphology and other factors (aerosols, breathing, etc.) can also be important [4].

 doi:10.20944/preprints202403.1863.v1

Current methods to generate respiratory airway models include computer-aided design (CAD), segmentation of medical images, and algorithm-based morphing [5]. The CAD-based approaches historically include Gambit and SolidWorks to generate new geometries, and HyperMorph, MAYA, and/or Blender to modify existing geometries [6]. Zhao et al. [7] and Talaat et al. [8] used user-defined functions (UDFs) to control the opening/closing of the glottis and expansion-contraction of the alveoli following the tidal breathing waveforms. Wang et al. [9] used a multi-point approach in MAYA to control the boundary motions such as the uvula flapping. Similar methods have also been applied in hydrodynamics of fish fins and aerodynamics of insect wings [10,11]. The segmentation method used computed tomography (CT) scans and magnetic resonance imaging (MRI) scans to reconstruct anatomically accurate, patient-specific airway models [12]. With quick advances in both imaging and segmentation techniques, this approach has become mainstream in airway model development in recent years, starting from relatively simple geometries such as the trachea to increasingly more sophisticated structures such as the nose and deep lungs [13–17]. Image segmentation has also been used to develop respiratory airway models in other species, with an emphasis on lab animals like mice, rats, rabbits, dogs, and monkeys to decrease animal usage [18–24]. However, this approach has been limited by ethical issues, low image resolutions, and data availability to meaningfully study the shape variation effects [25,26].

Tongue variability among subjects during inhalation drug delivery: The tongue position can significantly affect the upper airway geometry and airflow dynamics during inhalation, which is crucial for effective drug delivery to the lungs [27]. The variability in tongue position among subjects during inhalation drug delivery can be attributed to several factors. First, the size, shape, and position of the tongue, as well as the dimensions of the oral cavity, vary considerably among individuals. These anatomical differences can lead to differences in tongue positioning during inhalation. Second, breathing patterns, such as nasal vs. oronasal or shallow vs. deep breathing, can influence the tongue position. The coordination of the muscles involved in breathing maneuvers, including the genioglossus, hyoglossus, and styloglossus muscles, can vary among individuals and activities. Third, the posture and head position during drug delivery can also affect the positioning of the tongue and the pharyngeal morphology [28]. Other factors contributing to tongue position variability include age, health (e.g., obesity), medical condition (e.g., obstructive sleep apnea), medication use (e.g., sedatives or muscle relaxants), and inhalation devices (DPI, MDI, and nebulizer) [29–31]. The variability in tongue position can impact the airflow patterns, particle deposition, and overall effectiveness of inhaled drug delivery [32]. Considering this variability is key to optimizing inhalation drug delivery techniques and devices to ensure consistent and efficient delivery to the targets within the respiratory tract.

The adjoint solver was proposed in the 1970s in the field of aerodynamics, particularly in the context of aircraft design optimization [33]. The adjoint method has the advantage of efficiently computing the system performance with respect to shape design variables. Its earliest applications involved the design optimization of transonic airfoils and wings. By using the adjoint solver, researchers could efficiently compute the sensitivity of aerodynamic quantities (such as drag or lift) to changes in the shape of the airfoil or wing. This information was then used in optimization algorithms to iteratively modify the shape and improve the aerodynamic performance [34,35]. Since its inception, the adjoint solver has found applications in various other fields, including structural optimization, inverse design problems, shape optimization, and multiphase flows [36–39]. Note that the observables in the adjoint solver requires field variables, such as velocity, pressure, and temperature to compute the adjoint sensitivity, thus precluding its usage in simulations of inhalation drug delivery, where aerosols were often considered as the discrete phase [40]. One exception is when aerosols are treated as the chemical species or probability density, the concentration or probability are field variables, and thus can be used to construct design observables for adjoint sensitivity calculation and shape optimization.

The objective of this study is to evaluate the feasibility of using adjoint solver to study the morphology sensitivity to inhalation dosimetry of inhaled vapor or nanomedicine to the mouth-tongue morphology. A CFD with wall adsorption (physiology-based pharmacokinetics, PBPK) was

 doi:10.20944/preprints202403.1863.v1

employed and two chemical species, Acetaldehyde and Benzene, were considered. Specific aims included:

1. Develop an adjoint-based CFD-PBPK model for vapors and nanomedicines.
2. Evaluate the sensitivity of the filtration efficiency to the airway shape.
3. Optimize the airway shape for prescribed species-specific filtration efficiencies.

2. Methods

2.1. Study Design

An adjoint-CFD solver used in this study consists of three components: a flow solver, an adjoint solver, and morphing, which is followed by an optimization loop (Figure 1). The flow solver simulates the flow/vapor fields in the upper airway based on inputs and computes the objective function or observable (exiting vapor flux). The adjoint equations solve for shape sensitivity and modify the geometry according to a prescribed target for the observable. The updated observable is compared to the target, and the above process will continue until the target is reached.

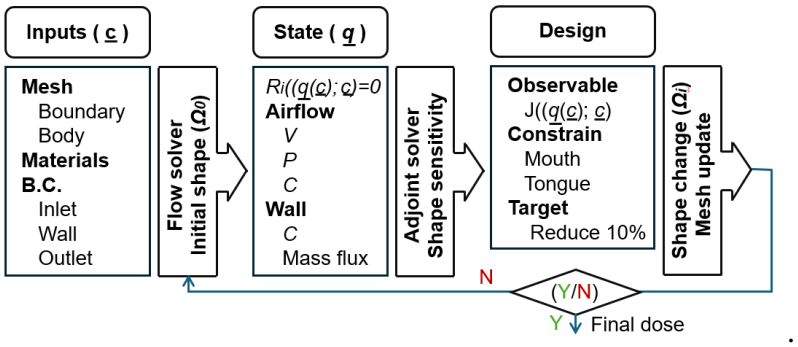

Figure 1. The adjoint-CFD solver with three phases: flow solution, adjoint solution, and design.

A mouth-tongue-throat model that had been previously developed in [41] was used to evaluate the airway morphological impacts on inhalation dosimetry (Figures 2a&b). Specifically, the effects of tongue shape and position on vapor filtration were investigated using the adjoint method. To study the vapor filtration at different tongue positions, the observable in the adjoint equation was defined as the surface integral of the vapor concentration at the tracheal outlet (i.e., the exiting mass flux). Adjoint outputs include shape sensitivity and normal displacement. Due to the large range of sensitivity variation, the shape sensitivity magnitude at the log10 scale was adopted to visualize the sensitivity on the surface.

Automatic airway remodeling was realized was obtained by morphing mesh according to the calculated adjoint sensitivities and targeted optimization. Controls included zone selection, objective, design constraints, region, smoothness, and a number of optimizations. Polynomial interpolation method for defining new surface shapes based on the existing surface of the mouth and tongue. The optimization was carried out using the gradient-based optimizer. To evalaute the applicability and robustness of the adjoint solver, the airway geometry was modified until the resultant geometry was anatomically unrealistic or the computational mesh became unrepairable from negative cells.

To study the effects of different chemicals, two vapors, Acetaldehyde and Benzene, were considered in this study for their similar diffusivities but different solubility in liquids [42,43]. Both computional and analytical methods to study the transport and absorption of inhaled chemicals. To consider the differences between chemicals, an analytical wall boundary condition was developed at the air-mucus interface that included the solubilities and diffusivities in different media, as well as the thicknesses of the media.

Preprints.org (www.preprints.org) | NOT PEER-REVIEWED | Posted: 29 March 2024 doi:10.20944/preprints202403.1863.v1

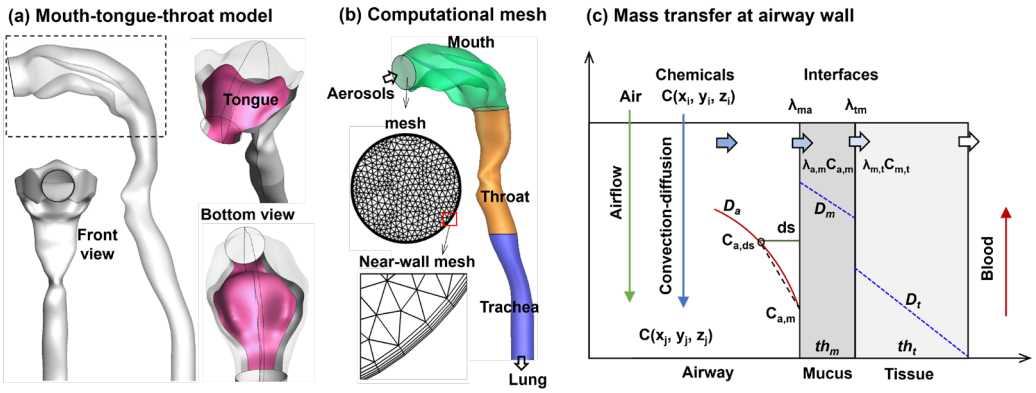

Figure 2. Models: (a) geometry model of mouth-tongue throat, (b) computational mesh, and (3) mass transfer at the airway wall with mucus, tissue, and blood.

2.2. Airflow and Vapor Transport

Airflows were assumed to be isothermal and incompressible. The Low Reynolds number (LRN) k-ω model was used to simulate respiratory airflow and vapor transport in the airway [44,45]. The LRN k-ω model has also been well validated to capture turbulent and transitional flows that featured human respirations [46–48]. The governing equations are [45],

$$\frac{\partial \overline{u}_i}{\partial x_i} = 0; \quad \frac{\partial \overline{u}_i}{\partial t} + \overline{u}_j \frac{\partial \overline{u}_i}{\partial x_j} = -\frac{1}{\rho}\frac{\partial p}{\partial x_i} + \frac{\partial}{\partial x_j}\left[\left(\nu + \nu_T\right)\left(\frac{\partial \overline{u}_i}{\partial x_j} + \frac{\partial \overline{u}_j}{\partial x_i}\right)\right] \tag{1}$$

here $\overline{u}_i$ is the airflow velocity components (i = 1, 2, and 3), ν is the viscosity, k is turbulent kinetic energy and ω is the specific dissipation rate (ω),

$$\frac{\partial k}{\partial t} + \overline{u}_j \frac{\partial k}{\partial x_j} = \tau_{ij} \frac{\partial \overline{u}_i}{\partial x_j} - \varepsilon_k + \frac{\partial}{\partial x_j}\left[\left(\nu + 0.5\nu_T\right)\left(\frac{\partial k}{\partial x_j}\right)\right] \tag{2}$$

$$\frac{\partial \omega}{\partial t} + \overline{u}_j \frac{\partial \omega}{\partial x_j} = \frac{13}{25}\frac{\omega}{k}\tau_{ij} \frac{\partial \overline{u}_i}{\partial x_j} - \varepsilon_\omega + \frac{\partial}{\partial x_j}\left[\left(\nu + 0.5\nu_T\right)\left(\frac{\partial \omega}{\partial x_j}\right)\right] \tag{3}$$

where τ_{ij} is the shear stress tensor [45]. The mass transport of the Chemical concentration (c) in the airflow and liquid are governed by diffusion and/or convection, which are expressed below,

$$\frac{\partial c}{\partial t} + \frac{\partial\left(u_j c\right)}{\partial x_j} = \frac{\partial}{\partial x_j}\left[\left(\tilde{D} + \frac{\nu_T}{Sc_T}\right)\frac{\partial c}{\partial x_j}\right] \tag{4}$$

here $\tilde{D}$ is the Chemical diffusivity in the medium and ScT is the Schmidt number (0.9).

2.2. Boundary Conditions at Air-Mucus Interface

Particles readily adhere to sticky airway surfaces upon contact, whereas vapors do not deposit or absorb entirely due to their finite solubility. The absorption of vapors from the air into another medium is governed by various factors, including solubility, diffusivity, and reactivity in both phases. These parameters are specific to the materials involved and must be determined through experimental investigations [49]. This study does not account for any chemical reactions. In steady-flow conditions, the rate of mass transfer per unit area (mass flux, $\dot{m}$) occurring at the air-liquid interface can be expressed as follows [50],

 doi:10.20944/preprints202403.1863.v1

$$\dot{m}_a = D_a \frac{\partial C_a}{\partial s} = D_a \frac{C_{a,ds} - C_{a,m}}{ds}; \qquad \dot{m}_m = D_m \frac{\lambda m_{ma} C_{a,m} - C_{m,t}}{th_m}; \qquad \dot{m}_t = D_t \frac{\lambda_{tm} C_{m,t} - 0}{th_t} \tag{5}$$

Here D_a, D_m, D_t are the avopr diffusivitiesin air, mucus, and tissue, *ds* represents the distance between the near-wall cell center and the interface, while th denotes the thickness of the liquid layer, as illustrated in Figure 2c. Due to the differences in chemical solubilities in air and liquid, there exists a discontinuity in the vapor concentration across the interface. This can be expressed as $C_{m,a} = \lambda_{ma} C_{a,m}$, where λ_{ma} is the air-mucus partition factor for the chemical. Based on the above equations, the chemical concentration at the interface in the air phase can be calculated as,

$$C_{a,m} = C_{a,ds} \frac{1}{1 + \mathrm{K}ds}; \qquad \mathrm{K} = \frac{D_t}{D_a} \frac{\lambda_{ma} \lambda_{tm} D_m D_t}{\left(D_m th_t + \lambda_{tm} D_t th_m \right)} \tag{6}$$

The transport properties of Acetaldehyde and Benzene are listed in Table 1 [50]. For a given medium, their diffusivities do not differ much. However, their partition factors are significantly different, with Acetaldehyde being two orders of magnitude higher than Benzene at the air-mucus interface, while being one order of magnitude lower than Benzene at the mucus-tissue interface (Table 1). Putting all transport parameters into eqn. 6, the kappa K was 117.73 for Acetaldehyde and 9.42 for Benzene. A user-defined function (UDF) was developed to account for the airway wall vapor concentration for different chemicals [50].

Table 1. Trasport properties of chemical vaoprs.

	D_a (cm^2/s)	λ_{ma}	D_m (cm^2/s)	λ_{tm}	D_t (cm^2/s)
Acetaldehyde	8.0×10^{-2}	3.2×10^{2}	8.0×10^{-6}	5.9×10^{-1}	2.64×10^{-6}
Benzene	8.8×10^{-2}	4.4	9.8×10^{-6}	4.1	3.23×10^{-6}

2.2. Adjoint State Euqation

The adjoint equations for fluid flows are derived from introducing adjoint variables into the Navier-Stokes equations [51–54]. These adjoint variables represent the sensitivity of a specific objective function, or observable to changes in the design variables, such as shape or material properties). Note that the boundaries, Ω determined the shape. The flow solution $\underline{q}$ with inputs $\underline{c}$ can be expressed as zero residuals of the Navier-Stokes equations, i.e., $R_i\left(\underline{q}\left(\underline{c}\right);\underline{c}\right) = 0$. For an observable $J\left(\underline{q}\left(\underline{c}\right);\underline{c}\right)$, which is a function of both the inputs and flow solution, the adjoint sensitivities can be expressed as,

$$\frac{dJ}{d\underline{c}} = \frac{d\underline{q}}{d\underline{c}}\left(\frac{\partial J}{\partial \underline{q}} + \underline{\tilde{q}}^T \frac{\partial R}{\partial \underline{q}}\right) + \frac{\partial J}{\partial \underline{c}} + \underline{\tilde{q}}^T \frac{\partial R}{\partial \underline{c}} \tag{7}$$

Here, $\underline{\tilde{q}}^T$ is the adjoint solution variables, such that,

$$\frac{\partial J}{\partial \underline{q}} + \underline{\tilde{q}}^T \frac{\partial R}{\partial \underline{q}} = 0 \quad \Rightarrow \quad \left[\frac{\partial R}{\partial \underline{q}}\right]^T \underline{\tilde{q}} = -\left[\frac{\partial J}{\partial \underline{q}}\right]^T \tag{8}$$

Thus, the adjoint sensitivity equation (7) was reduced to a linear problem,

$$\frac{dJ}{d\underline{c}} = \frac{\partial J}{\partial \underline{c}} + \underline{\tilde{q}}^T \frac{\partial R}{\partial \underline{c}} \tag{8}$$

The above equation was assessed at every mesh point within the computational model. When considering shape sensitivity, the computational mesh (*x*, *y*, *z*) serves as the input vector. The term on the left-hand side represents the overall sensitivity of J. The initial term on the right-hand side is the variation of J with respect to *x*, *y*, *z* at a given mesh node, while the second term is the change of

 doi:10.20944/preprints202403.1863.v1

J due to the flow solution. Note that $\partial J / \partial \underline{c}$ and $\partial R / \partial \underline{c}$ are computed using expressions derived from the definitions of the observables and the CFD discretized equations, respectively. The adjoint method makes it practical to compute the shape derivative in large-scale optimization. The algebraic multigrid (AMG) iterative approach is used to compute an approximate solution to the above equation [55].

2.4. Numerical Methods

ANSYS Fluent (Canonsburg, PA) was implemented to simulate the steady airflows within the upper airway at 30 L/min. The transport and absorption of inhaled chemical vapors were simulated by means of user defined scalers (UDS). The vapor concentration on the airway walls was considered using a user-defined function. Zero vapor mass flux was specified at the tracheal outlet. Space discretization of second-order accuracy was implemented for all transport equations. ANSYS ICEM CFD (Canonsburg, PA) was utilized to generate computational mesh (Figure 2b). Grid-independent studies were performed following Xi et al. [56]. Five mesh finnesses (0.6–2.6 million cells) were tested and the grid-independnet results were estalished at 1.8 million cells, which was used for vapor transport/absorption in this study (Figure 2b). A normalized residual of 1×10^{-6} was used for flow continuity and 1×10^{-18} for UDS.

Discrete adjoint equations were used in this study, which discretized the flow solver first and then discretized the adjoint equation on the same mesh. In this manner, better accuracy of CFD solutions can be obtained, especially for the turbulence problem [57]. Similar to the flow solver, the least square cell-based approach was selected for gradient, standard approach for pressure, and second order upwind differencing for momentum. The dissipation suppression scheme was used for stabilization.

Airway remodeling was realized by morphing the mesh according to the calculated design change. Polynomial interpolation methods were used to define new surface shapes. Before mesh morphing, the recommended modified geometry was previewed relative to the original mesh to ensure its physical reasonability. The design space (i.e., region) enclosed the oral cavity (mouth and tongue). Mobile motion and symmetric plane were enabled for x, y, z directions to allow for deformation in all directions. A residual of 1e-6 was used for adjoint continuity and 1e-18 for adjoint UDS.

3. Results

3.1. Control Cases

Figure 3 shows the vapor concentration fields within the airway, as well as the vapor concentration on the airway surface. Both chemicals show a decrease in concentration along the airway, exhibited by the tapering red zone in the mid-sagittal planes. However, Acetaldehyde decreases at a higher rate and thus has a higher absorption rate than Benzene. This is consistent with the higher solubility of Acetaldehyde in mucus (Table 1). Due to the higher wall absorption rate and quicker depletion, the concentration of Acetaldehyde on the wall is much lower than that of Benzene. It is also clear that the Acetaldehyde gradient for Acetaldehyde is larger. In addition, the Acetaldehyde concentration field appears more heterogeneous, indicating a higher sensitivity to local flows and anatomical details.

 doi:10.20944/preprints202403.1863.v1

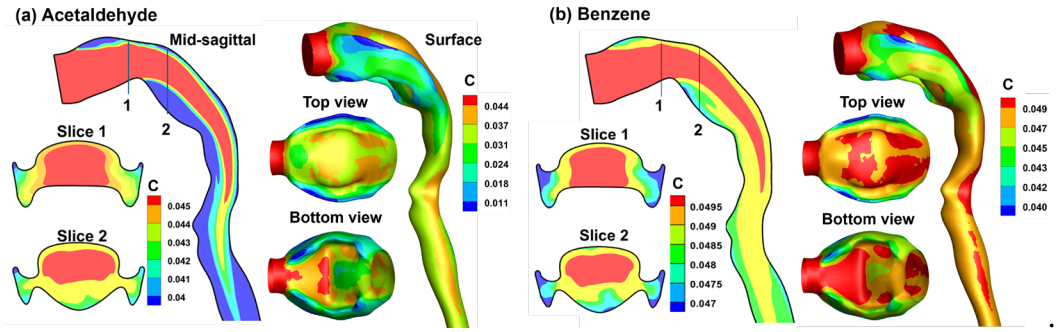

Figure 3. Vapor concentration in the core flows and on the wall surfaces for (a) acetaldehyde and (b) benzene. Different concentration ranges were used to highlight the concentration variation.

Figure 4 shows the adjoint sensitivity relative to the mouth-tongue morphology at log10 scale. Overall, larger shape sensitivity magnitudes are observed for Acetaldehyde than Benzene (Figures 4a vs. 4b). The sensitivity distributions are highly heterogeneous. Locally, higher sensitivities are observed at the mouth inlet, tongue (bottom view), and throat, while low sensitivities are observed at the lateral oral cavity and mouth roof (top view). The statistics of the shape sensitivities over the entire airway are shown as histograms in the right panels of Figures 4a and 4b, for Acetaldehyde and Benzene, respectively, both of which exhibit an approximate normal distribution.

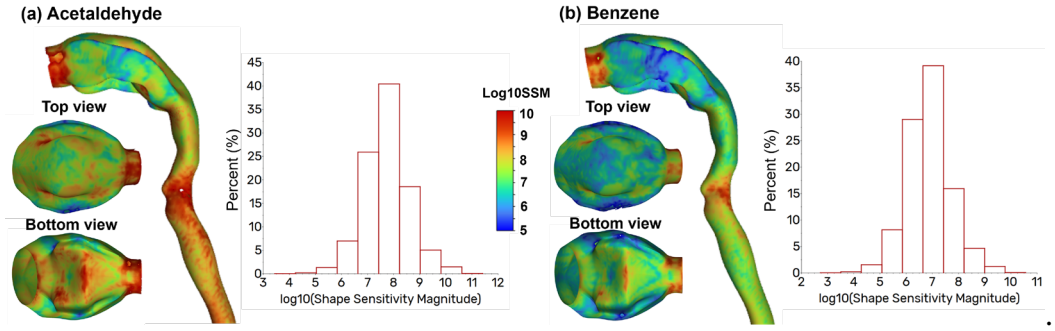

Figure 4. Adjoint shape sensitivity at log10 scale: (a) Acetaldehyde, and (b) Benzene.

3.2. Adjoint-Modified Aiway Models with varying Observale Targets

Figure 5 shows the modified mouth-tongue morphologies (red) specific to a target variation in the observable in comparison to the control (green). The first row shows the mouth roof (top view), the second row shows the tongue (bottom view), and the third row shows the lateral view of the oral cavity. Recall that the observable, which must be a field variable, is defined as the surface integral of the vapor concentration at the tracheal outlet, being equivalent to the mass flux escaping the filtration by the upper airway and entering the lung. The cases of decreasing the exiting mass flux by 1.2% (i.e., -1.2%) or increasing by 2% (i.e., +2%) are those with successful geometry/mesh modifications. Targets beyond this range for Acetaldehyde exit mass flux (i.e., -1.2 ~ +2%) have led to failed mesh with negative cell volumes. Likewise, the adjoint solutions for Benzene with exiting mass flux are limited to -0.12% to +0.15%, indicating a small design space to control Benzene uptake, as well as a smaller dosimetry variability for Benzene than Acetaldehyde.

 doi:10.20944/preprints202403.1863.v1

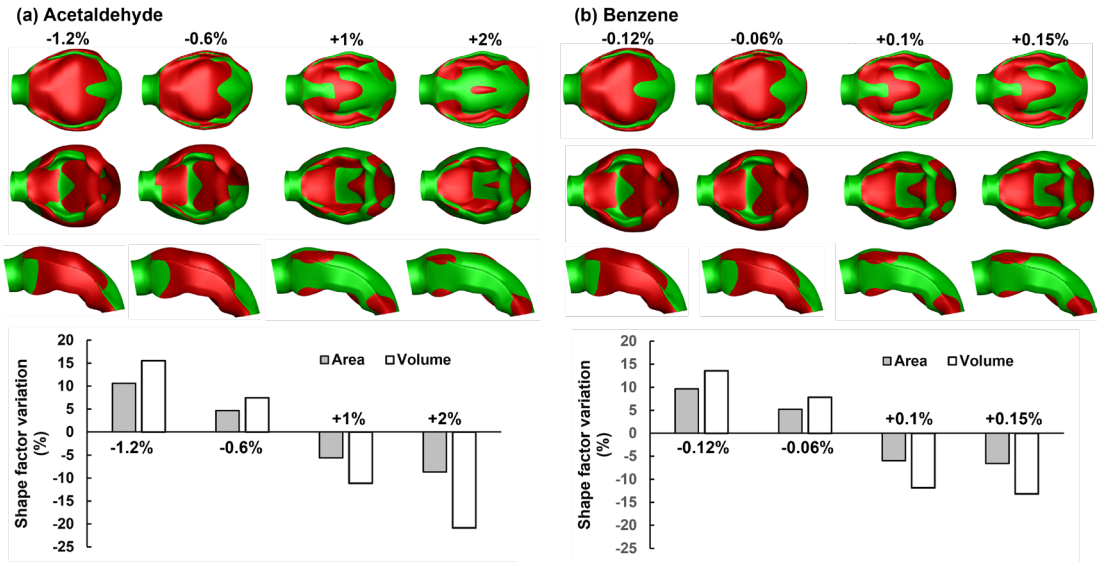

Figure 5. Comparison between original and adjoint-modified airway models with four different observable targets in terms of 3D morphology and dimension variation: (a) Acetaldehyde, and (b) Benzene.

The lower panels of Figure 5 compare the variation in morphological dimensions (area and volume) among the four models with different observable targets. Increasing the oral cavity volume/surface area decreases the exiting mass flux for both chemicals. This decrease may result from a longer residence time to interact with the wall or a larger surface area for absorption. Moreover, the volume varies at a much higher ratio than the surface area (lower panels, Figure 5).

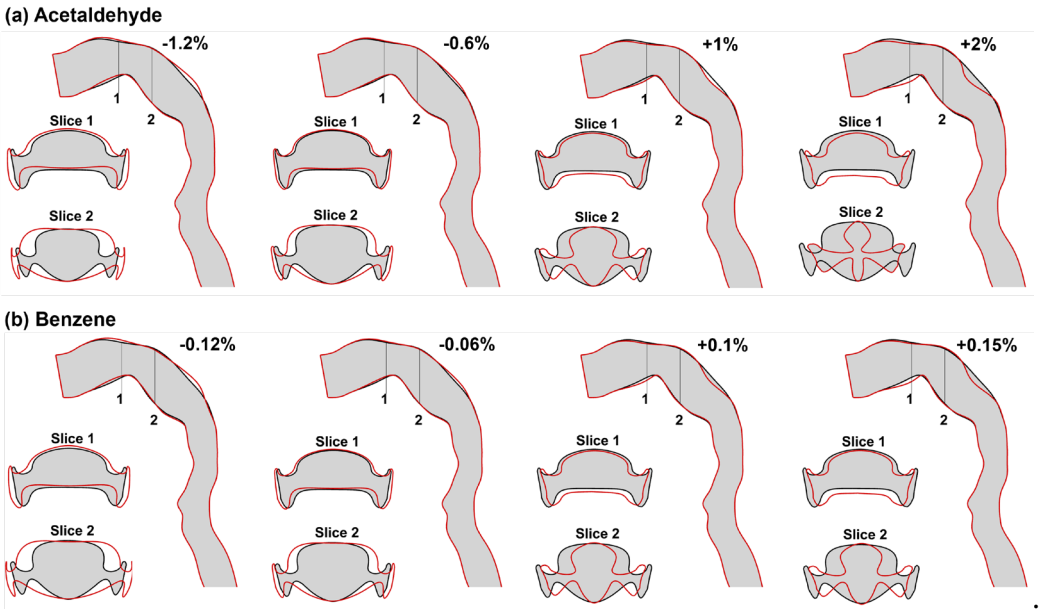

Figure 6. Comparison of the 2D contours between original and adjoint-modified airway geometries with four different observable targets: (a) Acetaldehyde, and (b) Benzene.

The four shape variants for Acetaldehyde and Benzene are further shown in Figure 6 in 2D plots with the mid-sagittal plane and two coronal slides. The filled gray represents the control case, while the red line represents the adjoint-morphed geometry. Two observations are notable. First, Slice 1 experienced limited morphing for all cases considered, while Slice 2 underwent drastic changes, particularly with the target of increasing mass flux exiting the upper airway. In particular, the case that increased the exiting concentration of Acetaldehyde by 2% (+2% for short) resulted in severe

 doi:10.20944/preprints202403.1863.v1

constriction in the back oral cavity (right panel, Figure 6a). This geometry was deformed to a level that was likely beyond the physiological feasibility. Second, the geometrical variation patterns appear similar between Acetaldehyde and Benzene for any of the first three columns (i.e., Acetaldehyde: -1.2% vs. Benzene: -0.12%, Figure 6). Considering that the geometry modification is determined by adjoint sensibility and target observables, this similarity indicates the overall alikeness in adjoint-determined shape normal sensitivity between Acetaldehyde and Benzene, in addition to the local discrepancies as shown in Figure 5.

3.3. Flow Fields in Adjoint-Modified Airway Models

The velocity fields in the adjoint-morphed oral airways from the Acetaldehyde control case are shown in Figure 7. Different color codes are used for the coronal and sagittal planes, reflective of their large differences in velocity ranges. Because the sagittal plane cuts through the main flow, while the coronal slices cut through the transverse secondary flows, the velocity range is 0–3 m/s for the sagittal plane and 0–1 m/s for the two coronal slices.

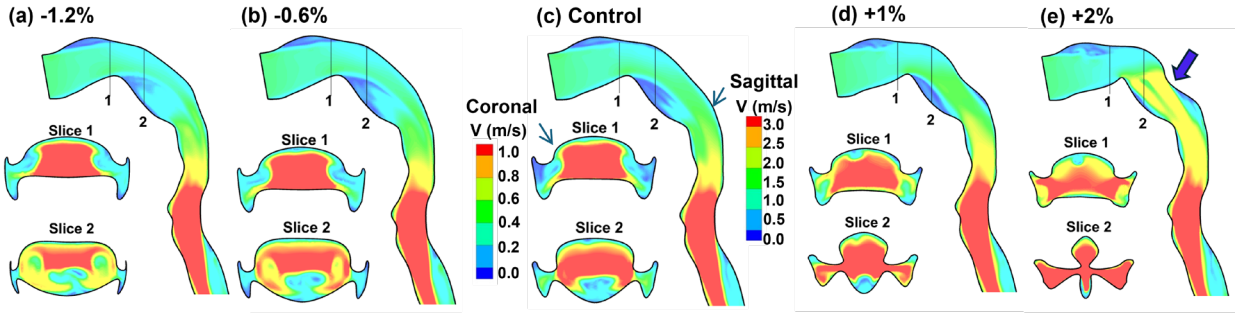

Figure 7. Airflow fields in modified airway models with different targets in Acetaldehyde exit mass flux: (a) -1.2%, (b) -0.6%, (c) control, (d) +1%, and (e) +2%.

Clear differences exist among the five models in both the mid-sagittal plane and the two coronal slices. From Figures 7a to 7e, the exit mass flux of Acetaldehyde progressively increases. The oral cavity becomes increasingly constricted at the back, accelerating airflow in the oropharyngeal region (blue arrow). At the same time, the core flow intensity constantly increases because of a gradual airway constriction, as indicated by the red-color zone in Slice 2. The flow dynamics in the modified geometries with Benzene are similar and are thus not presented.

Figure 8 shows the vortex structures in terms of Q-criterion within the airway, as well as two coronal slices. Note that the 3D iso-surfaces of the Q-criterion are colored by velocity, while the cross-sectional contour in the two coronal slices is colored by the Q-criterion per se in the range from -4000 to 4000. In the most constricted case (i.e., +2%), the cortices are significantly intensified in the oropharyngeal region than the other three due to the high flow speed. Comparing the Q-contour in the coronal slices, vorticity pairs are noted in the two larger oral cavities (i.e., -1.2% and -0.6% in Figures 8a and 8b), particularly in Slice 2. These vortices may increase the residence time of the vapor, increasing its chance of being absorbed by the mucus.

 doi:10.20944/preprints202403.1863.v1

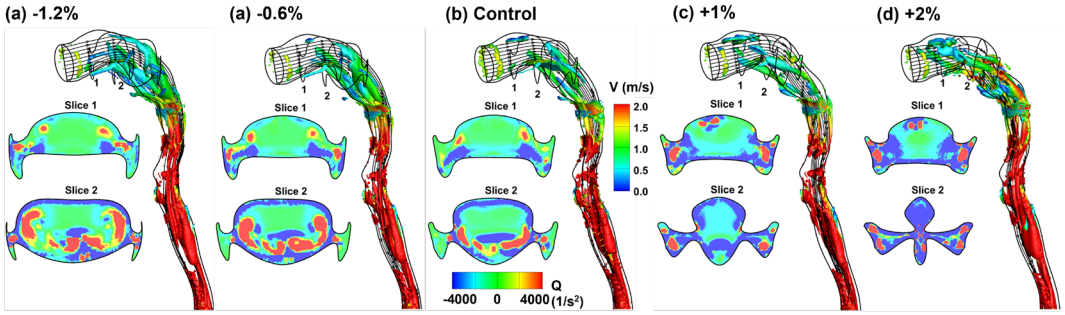

Figure 8. Iso-surfaces of Q-criterion in modified airway models with different targets in Acetaldehyde exit mass flux: (a) -1.2%, (b) -0.6%, (c) control, (d) +1%, and (e) +2%.

3.4. Vapor Transport and Wall Concentration in Adjoint-Modified Airway Models

The vapor transport in the modified oral airways is shown in Figure 9 in four models, whose exit mass flux increases from the left (i.e., -1.2%) to the right (+2%). Considering Acetaldehyde in Figure 9a, a high concentration of Acetaldehyde enters the mouth and tapers off due to diffusion, advection, and wall absorption. Dispersions are apparent in the oral cavity, which is featured by an abrupt expansion after the mouth opening. The secondary flows divert the Acetaldehyde vapor laterally toward the cheeks, further diluting the vapor concentration. However, the adjoint-morphed geometries from the left to the right successfully delayed the tapering process and prolonged the penetration depth of the vapor.

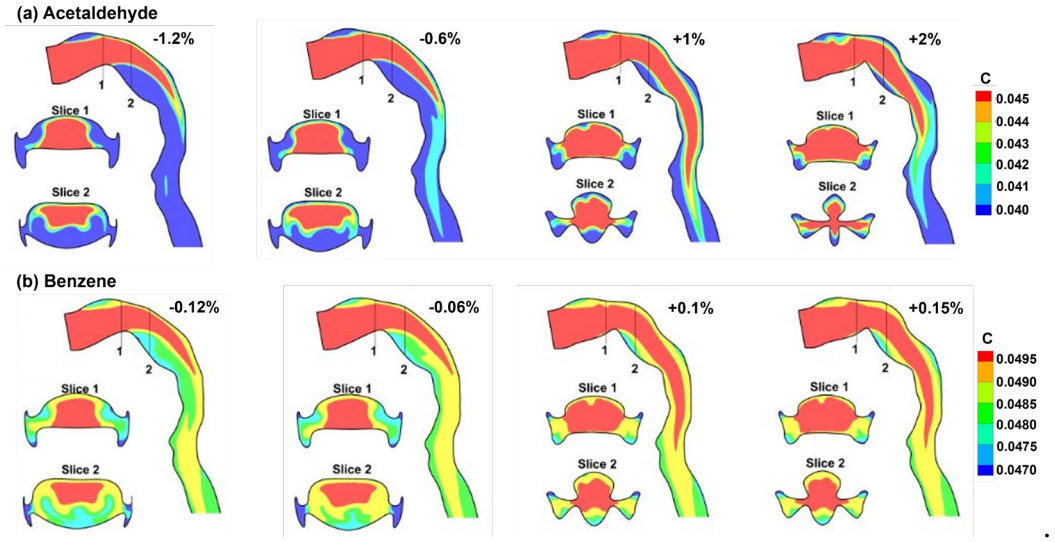

Figure 9. Vapor transport in modified airway models with different targets for the exit mass flux relative to the control case: (a) Acetaldehyde, and (b) Benzene.

Considering Benzene (Figure 9b), very different patterns and magnitudes from those of Acetaldehyde are observed in both the midsagittal plane and two coronal slices. Note that the color code is 0.0470–0.0495 for Benzene, which is much higher than that of Acetaldehyde, 0.040–0.045 (Figures 9b vs. 9a). When comparing the vapor pattern from left to right, the modified geometries progressively increase the vapor penetration depth. However, due to its relatively low absorption rate, the vapor concentration is consistently higher than that in Figure 9a. The gradient of Benzene concentration is lower, as indicated by the continuous, similar colors in the near-wall region, in contrast to the drastic color transition from red to blue for Acetaldehyde (Figure 9a).

Vapor concentrations on the airway wall are shown in Figure 10 in four modified airway geometries with increasing exit mass fluxes. Again, the oral cavity becomes narrower and more

 doi:10.20944/preprints202403.1863.v1

constricted in the models from the left to the right. Simultaneously, the shape of the mouth roof and tongue evolve, appearing to be more irregular from the case of "-1.2%" to "+2%". The vapor concentration on the lateral oral cavity (blue arrow, Figure 10a) is apparently higher at the "+2%" case than the cases of "-1.2%" and "-0.6%", which constitutes a lower concentration gradient and thus a lower absorption rate (Figure 10a). Considering the top view (mouth roof), the wall concentration on the back mouth increases, thus reducing the vapor concentration gradient and slowing vapor absorption. Similarly, the high-concentration zone on the tongue (bottom view) shifts from the front to the back, slowing the absorption-induced vapor depletion.

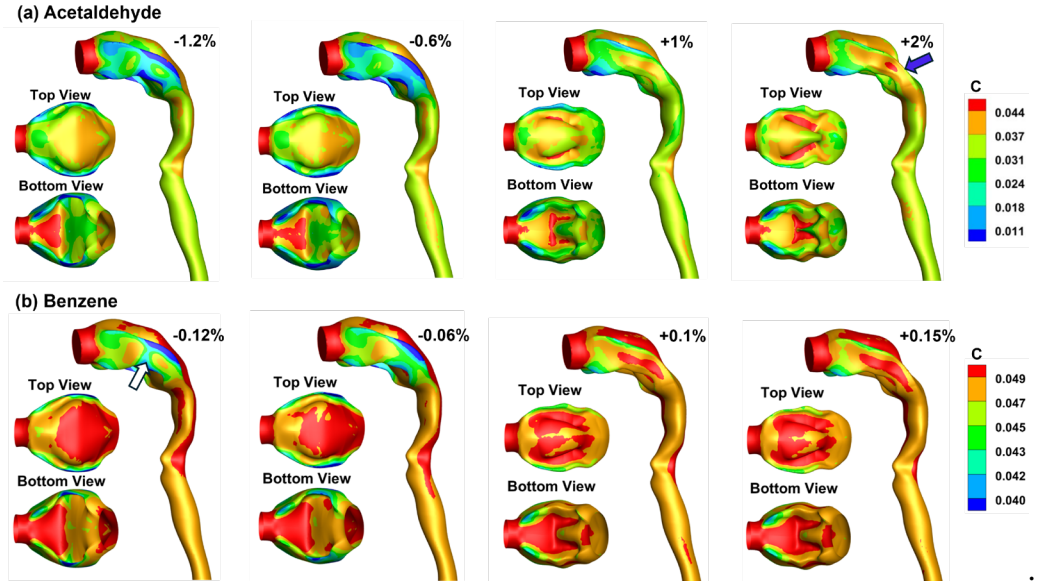

Figure 10. Vapor concentration distributions on the wall surfaces in modified airway models: (a) Acetaldehyde, and (b) Benzene.

Large differences exist in the wall vapor concentration between Benzene and acetaldehyde, as evidenced by the overall red color in Figure 10b vs. the greenish yellow in Figure 10a. The color code in Figure 10b ranges from 0.040 to 0.049, which is significantly higher than that of 0.011–0.044 in Figure 10a, especially for the lower end. Comparing the four cases in Figure 10b reveals that modifying the oral cavity with a similar magnitude as in Figure 9a generates a much smaller change in the wall vapor concentration, limiting the potential to effectively reduce vapor absorption. For Benzene (Figure 10b), the region with the most vapor concentration change is the lateral oral cavity or the lumen between the teeth and check (white arrow).

Figure 11 examines the correlation between the flow resistance and observable in adjoint-modified airway models with different target observables. Again, Acetaldehyde shows a higher sensitivity to pressure drop than Benzene (Figures 11a vs. 11b), consistent with the observations in Figures 9 and 10. Also, the potential for vapor uptake control through varying flow resistance is much smaller for Benzene than for Acetaldehyde (Figure 11c).

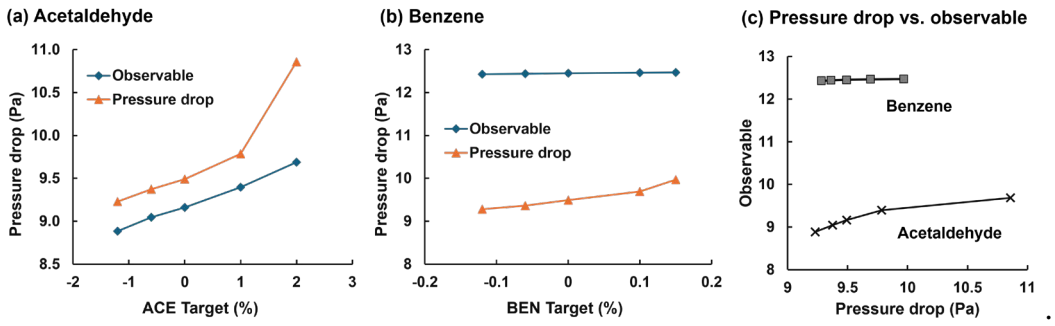

 doi:10.20944/preprints202403.1863.v1

Figure 11. Correlation between flow resistance and observable: (a) Acetaldehyde, (b) Benzene, and (c) pressure drop vs. observable.

4. Discussion

In this study, we explored the adjoint-CFD approach in studying the effects of mouth-tongue shape on the dosimetry of orally inhaled vapors. A practical method to study the influences of morphological variations on aerosol transport and deposition can open a new door to understanding drug bioavailability and bioequivalence among different subjects and between health and disease [58–61]. Despite large intersubject and intrasubject variability in respiratory anatomy, their effects on inhalation dosimetry have been historically less studied than other parameters, such as the flow rate and particle size. This has been attributed to challenges in varying the airway morphology while still keeping it physiologically realistic and representative. The results of this study demonstrate that the adjoint solver can provide a practical approach to examining the impacts of morphological factors. The adjoint sensitivity identified the most important factors affecting the vapor dosimetry, allowing exploration of mouth-tongue shape variations to minimize or maximize the vapor uptake in the upper airway (Figures 9-11). Instead of remodeling the airway geometry and solving the problem multiple times, the adjoint solver computes the observable gradient with respect to mesh points (shape sensitivity) by solving an additional set of equations (adjoint equations) only once. The structural modification can be a consequence of node displacements in a specific domain for a prescribed observable target, as shown in Figures 4–6). This makes the adjoint solver particularly powerful for inhalation dosimetry predictions, where the airway variability is tremendous, significantly reducing the computational cost compared to sensitivity analysis with individually modified airway models. Furthermore, detailed mechanisms for transport and deposition can also be explored after shape morphing by examining the shape variations and subsequent variations in flow/vapor dynamics (Figures 7–9)

Due to the automatic morphing capacity, this approach can be more user-friendly than other morphing methods based on CAD, image segmentation, mathematical algorithms (e.g., statistical shape modeling), or manual remodeling (e.g., Hypermesh, MAYA, Blender) [62]. Note that the statistical shape modeling needs a training database of airway shape models, which are difficult to obtain per se, let alone consistent shapes with desired variability. The HyperMorph modifies a shape by enclosing the region using a lattice and moving individual lattice points [63]. Even though it provides controlled shape remodeling, HyperMorph is labor-intensive and can generate unrealistic or unintended shapes due to the spline function [64]. By comparison, the adjoint solver does not need a training dataset and is automatic and controllable. It is also noted that the adjoint solver is optimization-orientated with a final output of static, optimized shapes; it is not suitable for dynamic shape variations as seen in fluid-structure interactions [65–67].

This study can be further improved by enhancing several simplifications, such as steady flow, oral airway only, rigid wall, and single observable. Inhalation dosimetry of chemical vapors and nanomedicines is sensitive to breathing maneuvers and can vary in different regions of the respiratory tract. An airway model extending beyond the oral airway can provide more realistic predictions of pulmonary dosimetry of orally inhaled aerosols. Including more bifurcations of the lung can even provide local or regional dosimetry in the lungs per se, providing granular information on bioavailability. Formulating and solving adjoint equations can be mathematically complex, and adapting existing simulation codes to include adjoint solvers can be challenging. Recall that the adjoint solver must use instantaneous field variables to constitute the observables (or objective function) for optimization. As a result, only a limited number of field variables are available, like pressure, velocity, temperature, and chemical species in the latest Fluent 23. Many field variables, as well as all discrete-phase variables, are still not available to be used for optimization. The level of geometry remodeling is also limited and susceptible to negative cells. In this study, the feasible control of the exiting mass flux is limited to “-1.2 – 2%” for Acetaldehyde and is even one order of magnitude lower for Benzene, “-0.12 – 1.5%, as shown in Figures 4&5.

 doi:10.20944/preprints202403.1863.v1

5. Conclusions

In summary, the hybrid adjoint-CFD model with a wall absorption model was demonstrated to provide a practical approach to explore mouth-tongue shape effects on vapor deposition. Similar efforts can be extended to other respiratory tract regions or the same region between health and disease or among different groups. The adjoint shape sensitivity analysis and optimization are significantly more efficient than conventional parametric analysis methods. However, at this stage, only continuous field variables can be used to constitute design observables to calculate the adjoint shape sensitivity; thus, the adjoint-CFD method is still infeasible for dosimetry control of discrete phase particles.

Author Contributions: Conceptualization, X.S. and J.X.; methodology, M.T. X.S., and J.X.; software, M.T. and J.X.; validation, X.S. and J.X.; formal analysis, M.T. X.S., and J.X.; investigation, M.T., X.S. and J.X.; data curation, M.T.; writing—original draft preparation, J.X.; writing—review and editing, M.T. and X.S.; visualization, M.T. and J.X.; supervision, J.X. All authors have read and agreed to the published version of the manuscript.

Funding: This research received no external funding.

Data Availability Statement: The data presented in this study are available upon request from the corresponding author.

Acknowledgments: Amr Seifelnasr at UMass Lowell Biomedical Engineering is gratefully acknowledged for editing and proofreading this manuscript.

Conflicts of Interest: The authors declare no conflict of interest.

References

1. Labiris, N.R.; Dolovich, M.B. Pulmonary drug delivery. Part I: physiological factors affecting therapeutic effectiveness of aerosolized medications. *Br. J. Clin. Pharmacol.* **2003**, *56*, 588-599.
2. Xi, J.; Walfield, B.; Si, X.A.; Bankier, A.A. Lung Physiological Variations in COVID-19 Patients and Inhalation Therapy Development for Remodeled Lungs. *SciMedicine J.* **2021**, *3*, 198-208.
3. Ochs, M.; Nyengaard, J.R.; Jung, A.; Knudsen, L.; Voigt, M.; Wahlers, T.; Richter, J.; Gundersen, H.J.G. The number of alveoli in the human lung. *Am. J. Respir. Crit. Care Med.* **2004**, *169*, 120-124.
4. Islam, M.S.; Paul, G.; Ong, H.X.; Young, P.M.; Gu, Y.T.; Saha, S.C. A review of respiratory anatomical development, air flow characterization and particle deposition. *Int. J. Environ. Res. Public Health* **2020**, *17*.
5. Kitaoka, H.; Takaki, R.; Suki, B. A three-dimensional model of the human airway tree. *J. Appl. Physiol.* **1999**, *87*, 2207-2217.
6. Wang, J.; Wainwright, D.K.; Lindengren, R.E.; Lauder, G.V.; Dong, H. Tuna locomotion: a computational hydrodynamic analysis of finlet function. *J R. Soc. Interface* **2020**, *17*, 20190590.
7. Zhao, J.; Feng, Y.; Fromen, C.A. Glottis motion effects on the particle transport and deposition in a subject-specific mouth-to-trachea model: A CFPD study. *Computers in Biology and Medicine* **2020**, *116*, 103532.
8. Talaat, M.; Si, X.A.; Tanbour, H.; Xi, J. Numerical studies of nanoparticle transport and deposition in terminal alveolar models with varying complexities. *Med One* **2019**, *4*, e190018.
9. Wang, J.; Xi, J.; Han, P.; Wongwiset, N.; Pontius, J.; Dong, H. Computational analysis of a flapping uvula on aerodynamics and pharyngeal wall collapsibility in sleep apnea. *J. Biomech.* **2019**, *94*, 88-98.
10. Zhong, Q.; Dong, H.; Quinn, D.B. How dorsal fin sharpness affects swimming speed and economy. *J. Fluid Mech.* **2019**, *878*, 370-385.
11. Koehler, C.; Liang, Z.; Gaston, Z.; Wan, H.; Dong, H. 3D reconstruction and analysis of wing deformation in free-flying dragonflies. *J. Exp. Biol.* **2012**, *215*, 3018-3027.
12. Vinchurkar, S.; De Backer, L.; Vos, W.; Van Holsbeke, C.; De Backer, J.; De Backer, W. A case series on lung deposition analysis of inhaled medication using functional imaging based computational fluid dynamics in asthmatic patients: effect of upper airway morphology and comparison with in vivo data. *Inhal. Toxicol.* **2012**, *24*, 81-88.
13. Lepley, T.J.; Frusciante, R.P.; Malik, J.; Farag, A.; Otto, B.A.; Zhao, K. Otolaryngologists' radiological assessment of nasal septum deviation symptomatology. *Eur Arch Otorhinolaryngol* **2023**, *280*, 235-240.
14. Corley, R.A.; Kabilan, S.; Kuprat, A.P.; Carson, J.P.; Minard, K.R.; Jacob, R.E.; Timchalk, C.; Glenny, R.; Pipavath, S.; Cox, T.; et al. Comparative computational modeling of airflows and vapor Dosimetry in the respiratory tracts of rat, monkey, and human. *Toxicol. Sci.* **2012**, *128*, 500-516.
15. Amjadimanesh, H.; Faramarzi, M.; Sadrizadeh, S.; Abouali, O. Micro-particle deposition in maxillary sinus for various sizes of opening in a virtual endoscopic surgery. *Exp. Comput. Multiph. Flow* **2023**, *5*, 262-271.
16. Wedel, J.; Steinmann, P.; Štrakl, M.; Hriberšek, M.; Ravnik, J. Can CFD establish a connection to a milder COVID-19 disease in younger people? Aerosol deposition in lungs of different age groups based on Lagrangian particle tracking in turbulent flow. *Comput. Mech.* **2021**, *67*, 1497-1513.

17. Shrestha, K.; Wong, E.; Salati, H.; Fletcher, D.F.; Singh, N.; Inthavong, K. Liquid volume and squeeze force effects on nasal irrigation using Volume of Fluid modelling. *Exp. Comput. Multiph. Flow* **2022**, *4*, 445-464.
18. Craven, B.A.; Neuberger, T.; Paterson, E.G.; Webb, A.G.; Josephson, E.M.; Morrison, E.E.; Settles, G.S. Reconstruction and morphometric analysis of the nasal airway of the dog (Canis familiaris) and implications regarding olfactory airflow. *Anat. Rec.* **2007**, *290*, 1325-1340.
19. Rygg, A.D.; Van Valkenburgh, B.; Craven, B.A. The influence of sniffing on airflow and odorant deposition in the canine nasal cavity. *Chem. Senses* **2017**, *42*, 683-698.
20. Corley, R.A.; Minard, K.R.; Kabilan, S.; Einstein, D.R.; Kuprat, A.P.; Harkema, J.R.; Kimbell, J.S.; Gargas, M.L.; Kinzell, J.H. Magnetic resonance imaging and computational fluid dynamics (CFD) simulations of rabbit nasal airflows for the development of hybrid CFD/PBPK models. *Inhal. Toxicol.* **2009**, *21*, 512-518.
21. Wu, Z.; Jiang, J.; Lischka, F.W.; McGrane, S.J.; Porat-Mesenco, Y.; Zhao, K. Domestic cat nose functions as a highly efficient coiled parallel gas chromatograph. *PLOS Comput. Biol.* **2023**, *19*, e1011119.
22. Dong, J.; Ma, J.; Tian, L.; Inthavong, K.; Ito, K.; Tu, J. Numerical analysis of nanoparticle transport and deposition in a cynomolgus monkey nasal passage. *Int. J. Numer. Method. Biomed. Eng.* **2021**, *37*, e3414.
23. Tian, L.; Dong, J.; Shang, Y.; Tu, J. Detailed comparison of anatomy and airflow dynamics in human and cynomolgus monkey nasal cavity. *Comput. Biol. Med.* **2022**, *141*, 105150.
24. Xi, J.; Si, X.A.; Malvè, M. Nasal anatomy and sniffing in respiration and olfaction of wild and domestic animals. *Front Vet Sci* **2023**, *10*, 1172140.
25. Tanabe, N.; Hirai, T. Recent advances in airway imaging using micro-computed tomography and computed tomography for chronic obstructive pulmonary disease. *Korean J. Intern. Med.* **2021**, *36*, 1294-1304.
26. Fernandez-Tena, A.; Fernandez-Francos, J.; Agujetas-Ortiz, R.; Casan-Clara, P. Airway model reconstructed from CT images. *Eur. Respir. J.* **2016**, *48*, PA4404.
27. Xi, J.; Yang, T. Variability in oropharyngeal airflow and aerosol deposition due to changing tongue positions. *J. Drug Deliv. Sci. Technol.* **2019**, *49*, 674-682.
28. Gurani, S.F.; Di Carlo, G.; Cattaneo, P.M.; Thorn, J.J.; Pinholt, E.M. Effect of head and tongue posture on the pharyngeal airway dimensions and morphology in three-dimensional imaging: a systematic review. *J. Oral Maxillofac. Res.* **2016**, *7*, e1.
29. Wang, S.H.; Keenan, B.T.; Wiemken, A.; Zang, Y.; Staley, B.; Sarwer, D.B.; Torigian, D.A.; Williams, N.; Pack, A.I.; Schwab, R.J. Effect of weight loss on upper airway anatomy and the apnea-hypopnea index. the importance of tongue fat. *Am. J. Respir. Crit. Care Med.* **2020**, *201*, 718-727.
30. Horiguchi, T.; Kondo, R. Determination of the preferred tongue position for optimal inhaler use. *J. Allergy Clin. Immunol. Pract.* **2018**, *6*, 1039-1041.e1033.
31. Zhou, X.; Li, Y.; Miao, H.; Zhang, Y.; Yu, A.; Huang, F.; Li, R.; Tong, Z. Numerical study on the effect of the realistic mouth-inhaler positions on orally inhaled drug delivery in pediatric intersubject upper airways. *Powder Technol.* **2024**, *432*, 119163.
32. Yang, T.; Si, X.; Xi, J. Sensitivity analysis and uncertainty quantification of nanoparticle deposition from tongue morphological variations. *Life* **2024**, *14*, 406.
33. Jansen, J.D. Adjoint-based optimization of multi-phase flow through porous media – A review. *Comput. Fluids* **2011**, *46*, 40-51.
34. Martins, J.R.R.A. Aerodynamic design optimization: Challenges and perspectives. *Comput. Fluids* **2022**, *239*, 105391.
35. Li, Z.; Zheng, X. Review of design optimization methods for turbomachinery aerodynamics. *Prog. Aerosp. Sci.* **2017**, *93*, 1-23.
36. Fikl, A.; Le Chenadec, V.; Sayadi, T. Control and optimization of interfacial flows using adjoint-based techniques. *Fluids* **2020**, *5*, 156.
37. Ancourt, K.; Peter, J.; Atinault, O. Adjoint and direct characteristic equations for two-dimensional compressible euler flows. *Aerospace* **2023**, *10*, 797.
38. Alexias, P.; Giannakoglou, K.C. Shape optimization of a two-fluid mixing device using continuous adjoint. *Fluids* **2020**, *5*, 11.
39. Basse, N.T. Flow-based optimization of products or devices. *Fluids* **2020**, *5*, 56.
40. Russell, T.F.; Celia, M.A. An overview of research on Eulerian–Lagrangian localized adjoint methods (ELLAM). *Adv. Water Resour.* **2002**, *25*, 1215-1231.
41. Lu, J.; Xi, J.; Langenderfer, J.E. Sensitivity analysis and uncertainty quantification in pulmonary drug delivery of orally inhaled pharmaceuticals. *J. Pharm. Sci.* **2017**, *106*, 3303-3315.
42. Tian, G.; Longest, P.W. Application of a new dosimetry program TAOCS to assess transient vapour absorption in the upper airways. *Inhal. Toxicol.* **2010**, *22*, 1047-1063.
43. Tian, G.; Longest, P.W. Transient absorption of inhaled vapors into a multilayer mucus–tissue–blood system. *Ann. Biomed. Eng.* **2010**, *38*, 517-536.
44. Ghalichi, F.; Deng, X.; Champlain, A.D.; Douville, Y.; King, M.; Guidoin, R. Low Reynolds number turbulence modeling of blood flow in arterial stenoses. *Biorheology* **1998**, *35*, 281-294.

 doi:10.20944/preprints202403.1863.v1

45. Wilcox, D.C. *Turbulence Modeling for CFD, 2nd Ed.*; DCW Industries, Inc.: California, 1998.
46. Zhang, Z.; Kleinstreuer, C. Low-Reynolds-number turbulent flows in locally constricted conduits: A comparison study. *AIAA Journal* **2003**, *41*, 831-840.
47. Zhang, Z.; Kleinstreuer, C. Airflow structures and nano-particle deposition in a human upper airway model. *Journal of Computational Physics* **2004**, *198*, 178-210.
48. Longest, P.W.; Vinchurkar, S. Validating CFD predictions of respiratory aerosol deposition: effects of upstream transition and turbulence. *J. Biomech.* **2007**, *40*, 305-316.
49. ICRP. *Human respiratory tract model for radiological protection*; Elsevier Science Ltd.: New York, 1994; Volume 66.
50. Tian, G.; Longest, P.W. Development of a CFD boundary condition to model transient vapor absorption in the respiratory airways. *J. Biomech. Eng.* **2010**, *132*, 051003.
51. Farazmand, M. An adjoint-based approach for finding invariant solutions of Navier–Stokes equations. *J. Fluid Mech.* **2016**, *795*, 278-312.
52. Gałecki, J.; Szumbarski, J. Adjoint-based optimal control of incompressible flows with convective-like energy-stable open boundary conditions. *Computers & Mathematics with Applications* **2022**, *106*, 40-56.
53. Popovac, M. Continuous adjoint topology optimization of duct flow configurations with explicit volume constraint for design variable update. *Energies* **2022**, *15*, 7349.
54. Grossberg, S.; Jarman, D.S.; Tabor, G.R. Derivation of the adjoint drift flux equations for multiphase flow. *Fluids* **2020**, *5*, 31.
55. Sbai, M.A.; Larabi, A. On solving groundwater flow and transport models with algebraic multigrid preconditioning. *Ground Water* **2021**, *59*, 100-108.
56. Xi, J.; Si, X.; Kim, J.W.; Berlinski, A. Simulation of airflow and aerosol deposition in the nasal cavity of a 5-year-old child. *J. Aerosol Sci.* **2011**, *42*, 156-173.
57. Stein, L.; Straube, F.; Weinzierl, S.; Lemke, M. Directional sound source modeling using the adjoint Euler equations in a finite-difference time-domain approach. *J Acoust Soc Am* **2020**, *148*, 3075.
58. Sun, Q.; Dong, J.; Zhang, Y.; Tian, L.; Tu, J. Numerical study of the effect of nasopharynx airway obstruction on the transport and deposition of nanoparticles in nasal airways. *Exp. Comput. Multiph. Flow* **2022**, *4*, 399-408.
59. Zare, F.; Aalaei, E.; Zare, F.; Faramarzi, M.; Kamali, R. Targeted drug delivery to the inferior meatus cavity of the nasal airway using a nasal spray device with angled tip. *Comput. Methods Programs Biomed.* **2022**, *221*, 106864.
60. Vinchurkar, S.; Vos, W.; Holsbeke, C.; Backer, J.D.; Poli, G.; Backer, W.D. The effects of extrafine beclomethasone/formoterol on hyperinflation and airway geometry in COPD patients. *Eur. Respir. J.* **2012**, *40*, P4833.
61. Si, X.; Xi, J.S.; Talaat, M.; Donepudi, R.; Su, W.-C.; Xi, J. Evaluation of impulse oscillometry in respiratory airway casts with varying cbstruction phenotypes, locations, and complexities. *J. Respir.* **2022**, *2*, 44-58.
62. Talaat, M.; Si, X.A.; Dong, H.; Xi, J. Leveraging statistical shape modeling in computational respiratory dynamics: Nanomedicine delivery in remodeled airways. *Comput. Methods Programs Biomed.* **2021**, *204*, 106079.
63. Xi, J.; Wang, Z.; Si, X.A.; Zhou, Y. Nasal dilation effects on olfactory deposition in unilateral and bi-directional deliveries: In vitro tests and numerical modeling. *Eur. J. Pharm. Sci.* **2018**, *118*, 113-123.
64. Xi, J.; Zhao, W. Correlating exhaled aerosol images to small airway obstructive diseases: A study with dynamic mode decomposition and machine learning. *PLoS One* **2019**, *14*, e0211413.
65. Menzer, A.; Gong, Y.; Fish, F.E.; Dong, H. Bio-inspired propulsion: towards understanding the role of pectoral fin kinematics in Manta-like swimming. *Biomimetics* **2022**, *7*, 45.
66. Gong, Y.; Wang, J.; Zhang, W.; Socha, J.J.; Dong, H. Computational analysis of vortex dynamics and aerodynamic performance in flying-snake-like gliding flight with horizontal undulation. *Phys. Fluids* **2022**, *34*.
67. Guo, J.; Zhang, W.; Han, P.; Fish, F.E.; Dong, H. Thrust generation and propulsive efficiency in dolphin-like swimming propulsion. *Bioinspir. Biomim.* **2023**, *18*, 056001.